Post-Print

Design, Manufacturing and Wind Tunnel Test of a Morphing Wing Based on Compliant Structures

Alessandro De Gaspari[*], Luca Riccobene[†] and Sergio Ricci[‡]
Politecnico di Milano, Via La Masa 34, 20156 Milano, Italy

The paper describes the activities performed at Politecnico di Milano in the framework of FP7–NOVEMOR Project aiming at the design, manufacturing and wind tunnel test of a wing model equipped with morphing leading and trailing edges based on compliant structures. Starting from the Reference Aircraft, i.e. a typical regional aircraft developed during NOVEMOR project, a small scale wind tunnel model has been derived to validate the proposed morphing concept and to correlate the numerical models in an experimental environment. A special attention has been devoted to the selection of the manufacturing technology due to the difficulty in realizing compliant structures with enough accuracy at a small scale level. After a short reminder of the tools developed for the design of variable camber morphing wings, the paper describes in details the design and manufacturing phases together with the functionality and wind tunnel tests. The results were used to validate the procedure adopted for the synthesis of the compliant structures and to evaluate the aerodynamic performances of the morphing wing.

Nomenclature

$\mathbf{a}$	=	vector of CST extra–coefficients
α	=	angle of attack [deg]
α_e	=	"effective" angle of attack [deg]
c	=	airfoil chord [m]
C_d	=	drag coefficient for unit span
C_l	=	lift coefficient for unit span
C_m	=	pitch moment coefficient for unit span
C_p	=	pressure coefficient

[*]Assistant Professor, Department of Aerospace Science and Technology, alessandro.degaspari@polimi.it.
[†]Post–doctoral Researcher, Department of Aerospace Science and Technology, luca.riccobene@polimi.it.
[‡]Associate Professor, Department of Aerospace Science and Technology, sergio.ricci@polimi.it.

$\Delta\kappa$	=	curvature difference function between the initial and the deformed shape [1/m]
ΔL	=	length difference function between the initial and the deformed shape [m]
δ_{LE}	=	leading edge equivalent deflection [deg]
δ_{TE}	=	trailing edge equivalent deflection [deg]
ψ	=	non–dimensional airfoil chordwise coordinate
$\mathbf{T}_p$	=	*CST–Vandermonde matrix* of order p
σ_{axial}	=	axial stress due to the skin length variation [Pa]
σ_{bend}	=	bending stress due to the skin curvature variation [Pa]

I. Introduction

LOOKING at the extensive literature concerning morphing aircraft, it is evident that morphing is nowadays considered as one of the most promising candidate to guarantee the new challenging requirements defined by US and EU organizations [1–4] in terms of aircraft increased efficiency and reduction of environmental impact. The new recommendations for civil aircraft industry require to reduce their emissions per passenger kilometer ($CO2 < 50\%$, NOx $< 80\%$, noise $< 50\%$) until 2020. If combined with an air traffic that is increasing by 5% per year, it means that the specific fuel consumption must be reduced by 50% only in order to keep the emission level constant to today. In this view, it is believed that morphing structures in civil aircraft industry are able to contribute to these goals by increasing the global efficiency of aircraft over the entire flight envelope.

The term morphing includes a large amount of concepts involving aircraft configuration, aerodynamics, structure variability and so on, and during last 20 years different concepts appeared in the literature. A comprehensive review of morphing concepts for transport aircraft and unmanned aerial vehicles can be found in [5] and [6], respectively.

Many research applications concern the realization of morphing wings, and most of them deal with large scale geometry modifications, including variable span [7] and variable structural stiffness so to induce favorable aeroelastic coupling and improved twist control [8, 9]. However, the ability to modify the airfoil shape is still one of the promising technology, due to its potential capability to optimize selected aircraft performance index during the mission, like for example fuel burning. Of special interest are the concepts focused on variable camber leading edge [10, 11], trailing edge [12, 13] and full profile [14, 15]. Nevertheless, the design of this kind of devices does not represent an easy task and would require the availability of ad–hoc developed procedures able to tackle the conflicting requirements such as the high deformability requested to change the airfoil shape coupled to the load carrying capability and low weight. Indeed, there is the need

for a specific design tool that could assist the engineers in the design of the optimal internal structure able to guarantee the required shape changes with the most efficient use of the actuators. Indeed, despite the different numerical and experimental applications now available many technological challenges still remain to be solved: the actuator integration capability (both discrete and distributed) and the need for a highly elastic skin capable to withstand air loads together with an appropriate mechanism, to cite a few. Finally, durability, maintenance and certification are still open issues for the application of morphing solutions to real aircraft.

Starting from the first rough models shown in [16], an intensive research activity was born and continues today at Politecnico di Milano (PoliMi), aiming at the development of dedicated tools for the automatic design of morphing wings. Over the years, this activity focused on the optimization of compliant structures, able to change the wing camber along the flight envelope. Compliant mechanisms for leading and trailing edge are obtained using two main tools dedicated to the morphing aircraft design, named PHORMA (Parametrical sHapes for aerOdinamic and stRuctural Modelling of Aircrafts) and SPHERA (Synthesis of comPliant mecHanisms for EngineeRing Applications). The proposed approach is based on a compact formulation to describe the wing geometry coupled to a two levels optimization procedure [17]. The first level, covered by PHORMA, allows to determine the best deformed airfoil configuration as the most efficient aerodynamic shape which at the same time limits the requested energy to deform the airfoil skin. It leads to the definition of the optimal morphing skin deformation, before the compliant structure is known. In the second optimization level, implemented into SPHERA, the best internal structural configuration is obtained using a topology optimization tool based on genetic algorithms that synthesizes a compliant structure able to adapt itself for matching the optimal shape coming out from the first level. Both the topology of the internal load paths, and the size of the structural elements are considered as design variables during this second design level. Once the optimal morphing airfoil is obtained, the finite element models are automatically generated both for the single rib and for a complete wing section. Many numerical applications of this methodology have been reported in the framework of different European projects such as NOVEMOR [18] and SARISTU [19]. This paper reports the results of the first experimental validation of the proposed approach concerning a small scale wind tunnel model equipped with morphing leading and trailing edge. The model was designed and tested at Politecnico di Milano during the final part of NOVEMOR project which is one of the many projects promoted by the 7th European Framework Programme. Starting from the so called Reference Aircraft (RA), developed inside NOVEMOR project for the regional aviation segment, and used as a benchmark in order to evaluate the potential benefits that morphing devices can bring in terms of global performances [20], a small scale wing has been derived for the experimental validation of the proposed morphing concept [21].

The paper summarizes the results obtained during the wind tunnel tests and it is organized as follows. Section II describes the layout of the wind–tunnel model. Section III describes the first design level for the definition of the optimal morphing shape. Section IV reports the second design level for the synthesis of morphing devices, based on compliant structures, to be implemented on the Leading and Trailing Edge (LE and TE) of the wind tunnel model. Section V introduces the postprocessing of the results, from the optimal 2D morphing LE and TE to the complete Finite Element Models (FEM) and CAD models, for the validation of the results and the manufacturing of the solutions by 3D printing techniques. Sections VI and VII describe the wind tunnel model and summarize the experimental results collected during the wind tunnel test campaign, while section VIII draws the conclusions of the study.

II. Layout of the Morphing Wing Model

The aim of the experimental activity described in this paper and performed by PoliMi is to evaluate the accuracy and validity of the methodologies for the design of morphing Leading and Trailing Edge devices based on compliant mechanisms. In particular, two are the main goals of the wind tunnel model here proposed. At first to validate the implemented framework for the optimal design of the compliant structures in an experimental environment, then to validate the numerically performances obtained from the morphing shapes. Since the scaling–up of the results to the full scale aircraft is not the main objective of this work, the design of the wind tunnel model, in terms of size and structural configuration, is not driven by any aerodynamic or dynamic scaling law but mainly by the size of the available wind tunnel, and by the constraints posed by the selected manufacturing technology.

Aiming at this main goal, a small scale wind tunnel model has been designed, manufactured and tested in the low turbulence closed–loop subsonic wind tunnel at PoliMi, that features a 1 x 1.5 m test section and has a maximum speed of 55 m/s. To simplify the experimental apparatus, it was decided to build a scaled wing with no taper, proportioned to fit into the available chamber space along the span–wise direction. Considering the supporting equipment and wind tunnel built–in attachments, the maximum span of the model was restricted to 930 mm. Once fixed this value, the most suitable wing section, to be scaled down, has been selected on the Reference Aircraft and considerations on eligible test conditions consequently prescribed the chord dimension.

The selection of the wing section must guarantee a correct balancing between the fidelity in replicating Reference Aircraft target performances and an easy manufacturing of the test prototype. The selected airfoil is extracted from the wing station placed at 32.6 % spanwise because it is the innermost one which also instersects the morphing regions of both LE and TE, as shown in [22]. The inner sections are more suitable due to the available internal space which allows a more easy installation of the morphing devices.

4

From the aerodynamic point of view, the tests aim at analyzing the morphing concepts in terms of two–dimensional performance only, accordingly to the availability of a straight wing setup. To minimize three–dimensional effects on the model it was necessary to limit the chord value so to reach a sufficient aspect ratio. This aerodynamic requirement must be balanced with the demand of scaling up the airfoil as much as possible to avoid excessively small compliant mechanism thicknesses and load–paths, facilitating at the same time the housing of the necessary actuation systems. An acceptable compromise was found setting the scale factor to $1:10$, which finally resulted in a chord dimension equal to $c = 418\,\mathrm{mm}$ for the specific airfoil selected for testing.

Starting from this wing section, and from the related scale factor, the corresponding morphing layout has been sketched, as shown in Fig. 1.
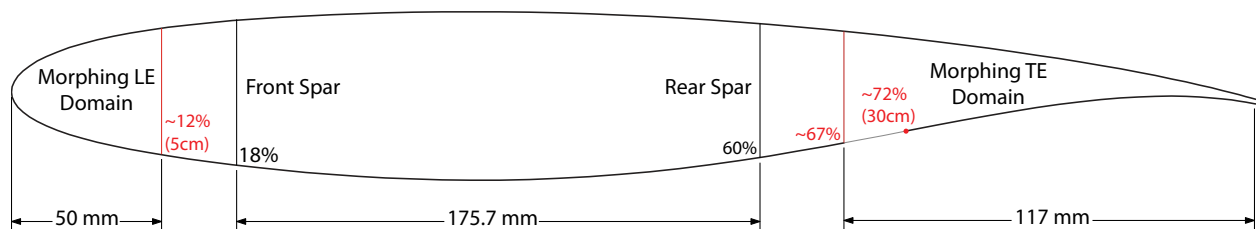

Figure 1   The layout of the morphing regions in the wind tunnel model.

Due to the scale factor adopted for the wing tunnel model a simple scaling down of the morphing devices already available for the Reference Aircraft is not a viable option. For this reason, a completely new design has been performed using PHORMA, for the morphing shape definition, and then SPHERA, for the synthesis of the compliant leading and trailing edge.

In general, the definition of the optimal 3D morphing shape by propagating an optimal 2D shape does not guarantee the obtainment of the best aero–structural configuration, especially in presence of significant aeroelastic deformations, even if by sure this approach simplifies the optimization problem. It must be pointed out that the developed framework is able to afford the morphing shape optimization both in 2D and in 3D: it is up to the user how to code the optimization problem. Since the wind tunnel model has a constant chord and a rigid wing, except for what concerns the LE and TE morphing components, and it is supported from both the end sections during the test, the 2D approach is believed more than acceptable in the application here described. The wind tunnel test can be actually considered as a 2D test.

The configuration of morphing LE and TE is strictly related to the manufacture technology and to the available material. The design of the compliant structures for the low–speed wind tunnel model represents a

challenge due to the need for exactly reproducing the compliance distribution at the reduced scale adopted. The selected technology is part of the Rapid Prototyping (RP) manufacture techniques and it has already been used to build wind tunnel models [23–25]. The idea was to be able to manufacture the complete morphing leading and trailing edge in a single piece, directly starting from the Computer–Aided Design (CAD) model.

Several materials and different RP technologies have been tested. SLA (Stereolithography) and SLS (Selective Laser Sintering) techniques, in combination respectively with the *Somos GP Plus*, which is a ABS–like material, and a fine powder on the basis of polyamide 12 (*PA 2200*), have been selected as the most suitable to manufacture compliant mechanisms. These materials have proved excellent capacity for flexibility combined with elasticity. Good results have been also obtained by Polyjet technology, but the final models showed a poor resistance to the environmental changes.

Afterwards, a 0.005 m thick compliant rib device has been manufactured in order to characterize the 3D printing materials. A test bench was set up to compare numerical and experimental deformations under the same actuation load. The mechanical properties were correlated by the same in–house FEM code embedded into SPHERA. Table 1 reports the actual mechanical properties, measured by experimental tests for material characterization, and used for the design of compliant devices.

Table 1   Mechanical properties used for the compliant mechanisms design.

Technical Data	
Tensile Strength	52 MPa
Elongation at break	24 %
Modulus of Elasticity	1.5 GPa
Poisson's Ratio	0.36
Flexural Strength	76 MPa
Flexural Modulus	1.4 GPa

According to the *distributed compliance* concept [17], the typical deformation of a compliant structure is characterized by a bending component much greater than the axial one. The flexural strength is used as stress constraint, instead of the tensile one, in both the shape optimization and the design of the compliant devices. During the shape optimization, the flexural strength is used to compute the maximum curvature difference $\Delta\kappa$ along the skin. During the design of the compliant devices, the stress constraint is activated only for the elements used to model the internal mechanism: the skin is excluded by the constraint computation because it is embedded into the definition of the optimal shape which is used as target.

III. Morphing Shape Design of the Wing Tunnel Model

The shape design of the wind tunnel model is based on a knowledge–based framework which is strictly linked to the PHORMA environment and it is able to define the optimal morphing shape to be used as target outlines, during the compliant mechanism generation. The embedded shape parameterization, is based on the CST (Class–Shape–Transformation) technique [26], and allows to take into account the skin structural response before the morphing mechanism has been defined. The same parameterization technique combines the estimation of the structural behavior of the morphing skin and the introduction of wing–box implicit constraint, representing a specific algorithm that allows to introduce only feasible perturbations that meet pre–assigned skin structural requirements [18]. This ability is based only on geometrical consideration: the axial stress (σ_{axial}), required to stretch or compress the skin, and the bending stress (σ_{bend}) can be directly deduced respectively by the length $\Delta L(x)$ and curvature $\Delta \kappa(x)$ difference functions between the initial and the deformed shape, with respect to $x = \psi \cdot c$. Once the skin structural constraints are satisfied, the aerodynamic mesh is produced and the CFD (Computational Fluid Dynamics) computations are performed. The generation of aerodynamic models is strictly connected to the same parametric description of the geometry.

After the airfoil was parametrically identified, the knowledge–based framework is coupled to an aero–structural shape optimization scheme. In this way, the procedure is able to follow a set of implicit rules governing the skin structural behaviour in order to prevent that the shape changes violate the skin structural requirements and the wing–box constraint during the optimization process.

Two different optimization problems were defined for the morphing LE and TE, for a single wind tunnel velocity equal to $40\,\mathrm{m/s}$: find the optimal morphing shape to minimize the C_d and maximize the C_l values, respectively. Both leading and trailing edge shape optimizations were performed for a constant value of $\alpha = 10\,\mathrm{deg}$, corresponding to the maximum angle of attack used during the wind tunnel tests. A special attention has to be devoted to the selection of skin structural constraints during the aerodynamic shape optimization. Indeed, the morphing LE and TE applied to the small scale of the model could potentially generate high values in terms of skin stress and deformation, making difficult the manufacturing process and the selection of the proper material.

A. Leading edge shape optimization

The leading edge optimization was run using an objective function that tries to minimize the drag at the maximum angle of attack attained in the wind tunnel. Since the best morphing shape generally corresponds to the maximum droop nose deflection in the high–lift conditions, the shape definition process is composed of different phases. In order to change the leading edge shape, a parametric model based on Bernstein Polynomials Order equal to $n = 10$ (BPO10) is generated before. Then, the leading–edge vertical position

is manually dropped until the maximum curvature difference is close to the limit value allowed by the skin properties, while the last $p = 8$ extra–coefficients are automatically computed to satisfy the wing–box implicit constraint [18]. After the leading–edge vertical position Z_{LE} is determined without violating the skin structural requirements, the droop nose shape is optimized from the aerodynamic point of view. The following shape optimization is defined including the same skin structural constraints applied before and keeping fixed the modified Z_{LE}:

1) *Objective function* (To minimize):

$$C_d \tag{1}$$

2) *Constraints*:

$$\mathbf{T}_8^T \mathbf{T}_8 \mathbf{a}^T = \mathbf{T}_8^T \mathbf{f}$$

$$\Delta \psi_{wing-box} \equiv (0.12, \ 1.)$$

$$C_l \geq 1.38$$

$$\mid \Delta L_{LE,skin} \mid = 0.$$

$$\max(\Delta \kappa) \leq 70 \, 1/\text{m}$$

3) *Variables*: $A_{up,1}$, $A_{up,2}$, $A_{low,1}$, $A_{low,2}$, R_{LE} and c

According to the optimization algorithm described in [18], the first term represents the implicit wing–box constraint which acts on the structural box region delimited by the front spar position and the end of the trailing edge, described by $l + 1$ pairwise distinct coordinates. If $\mathbf{T}_8$ represents the $(l + 1) \times 9$ *reduced CST–Vandermonde matrix*, $\mathbf{f}$ is the corresponding $(l + 1)$ vector. The unique solution of this linear system is equivalent to solve, in the least squares sense, the over–determined system that allows to compute the $p = 8$ extra–coefficients $\mathbf{a}$, given the $l + 1$ pairwise distinct real points, placed along the region which must be kept undeformed. The second constraint introduces the limits bounding this region, from the 12 % of the chord up to the end of the trailing edge.

In this way the perturbation affects only the domain outside the fixed regions. The optimization process acts on a subset of $(n - p = 2)$ extra–coefficient for the upper and the lower airfoil surfaces ($A_{up,1}$, $A_{up,2}$, $A_{low,1}$ and $A_{low,2}$), in addition to the leading–edge nose radius R_{LE} and the airfoil chord c which represent the degrees of freedom related to the boundary condition. The leading–edge vertical position Z_{LE} is preassigned as pointed out before. The main design rule from the skin structural point of view is keeping the circumferential skin length $L_{LE,skin}$ constant to avoid axial stress. A maximum curvature difference, between the undeformed and the morphing shapes, of 70 1/m have been adopted at this aim to control the maximum bending stress,

according to the material properties reported in Table 1.

B. Trailing edge shape optimization

The shape optimization procedure applied to the trailing edge works to maximize the morphing airfoil performances in terms of C_l improvement. Since the lift increment due to the trailing edge deflection can be considered constant in the linear portion of the $C_l = C_l(\alpha)$ curve, the objective function is computed for a single value of angle of attack during the optimization. The parametric representation adopted to change the trailing edge shape, is based on a Bernstein Polynomials Order equal to $n = 8$ (BPO8). The TE optimization problem is formulated as follows:

1) *Objective function* (To maximize):

$$C_l \tag{2}$$

2) *Constraints*:

$$\mathbf{T}_5^T \mathbf{T}_5 \mathbf{a}^T = \mathbf{T}_5^T \mathbf{f}$$

$$\Delta \psi_{wing-box} \equiv (0., \, 0.72)$$

$$| \, \Delta L_{TE,UpperSkin} \, | = 0.$$

$$| \, \Delta L_{TE,LowerSkin} \, | \leq 0.01 \cdot c$$

3) *Variables*: $A_{up,5}$, $A_{up,6}$, $A_{up,7}$, $A_{low,5}$, $A_{low,6}$, $A_{low,7}$, β, c and Z_{TE}

The implicit wing–box constraint affects the structural box region delimited by the leading–edge nose and the rear spar position placed at the $72\,\%$ of the chord and allows to compute the $p = 5$ extra–coefficients of the associated over–determined system. The optimization process acts on a total of 9 optimization variables represented by the subset of 3 extra–coefficients for both upper and lower surfaces ($A_{up,5}$, $A_{up,6}$, $A_{up,7}$, $A_{low,5}$, $A_{low,6}$ and $A_{low,7}$), in addition to the trailing–edge angle β, the airfoil chord c and the trailing–edge vertical position Z_{TE}. Different structural requirements were adopted for the trailing edge skin: the upper skin length constraint $\Delta L_{TE,UpperSkin}$ is set up to be constant to avoid axial stress, while the lower skin length constraint has been relaxed in order to obtain an efficient aerodynamic shape. This means that the lower skin is free to slide along its contour and corresponds to the introduction of a linear slider. The main design rule from a structural point of view is keeping $\Delta L_{TE,LowerSkin}$ smaller than $4\,\mathrm{mm}$.

C. Shape optimization results

The algorithm selected for solving this kind of optimization problems is a Sequential Quadratic Programming (SQP) algorithm. A different optimization algorithm, based on interior point techniques, has been tried, but

it has showed to suffer from the so–called local minima problem and to be slower than the SQP, when applied to this kind of morphing shape problem. Since the simplified geometry of the wind tunnel model leads to 2D aerodynamic models, the aerodynamic problem was solved using a specific code embedded into the CST code [18]. It is able to automatically produce structured D–meshes suitable to perform Reynolds–Averaged Navier–Stokes (RANS) computations, based on $k - \omega$ turbulence model. This kind of mesh is automatically produced around the parameterized airfoil by a script based on Ansys ICEMCFD [27] and it is already shown in [18], where the scheme of the whole simulation procedure is also reported. Concerning the wind tunnel model, dedicated convergence studies led to meshes composed of 41000 elements.

The following optimal morphing shapes have been identified at the end of the first design level. They will be used, as target shapes, in the design of the compliant leading and trailing edge:

- Maximum downward droop angle for the Leading Edge, corresponding to $\delta_{LE} = 7 \deg$ ($mLEc12$);
- Maximum upward and downward angle for the Trailing Edge, corresponding to $\delta_{TE} = \pm 10 \deg$ ($mTEc72up$ and $mTEc72down$).

where the equivalent deflections are conventionally defined as in [18].
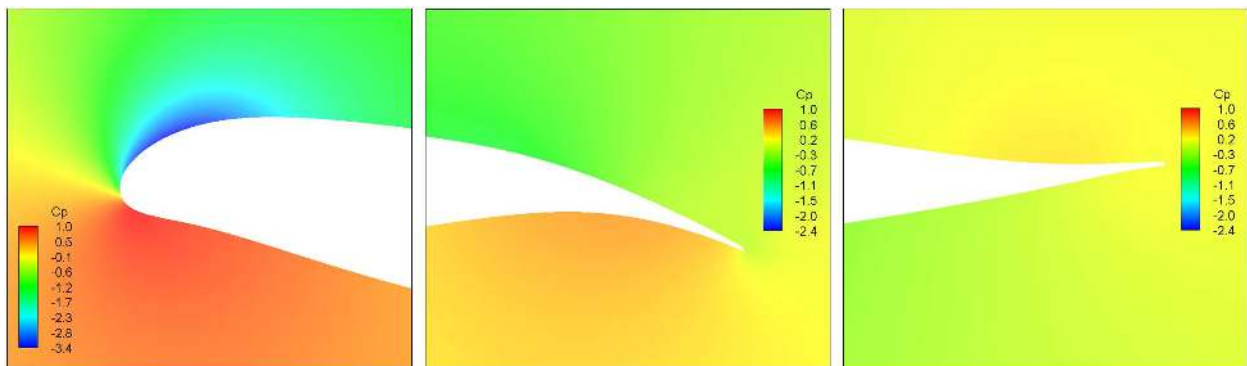
Figure 2 Aerodynamic results (RANS) in terms of C_p distribution around the optimal morphing shapes.

Corresponding aerodynamic results are shown in Figure 2 in terms of C_p distribution around the optimal morphing airfoils, for a wind tunnel test speed equal to $40 \, \mathrm{m/s}$. Although many more (CFD) analyses to compute complete polar curves were performed, two different angles of attack, considered in Table 2, were used during the design of corresponding compliant mechanisms.

IV. Design of Morphing Compliant Devices

As already mentioned the need for completely redesigning the morphing structures, able to work in a satisfactory way in spite of the small size of the experimental setup, is due to the impossibility to simply downsize the compliant solutions intended for the real Reference Aircraft. The starting point for the design of scaled

Table 2   Computational results in terms of aerodynamic coefficients of the optimal morphing shapes for a wind tunnel test speed equal to $40\,\mathrm{m/s}$ **and** $\alpha = 2\deg/10\deg$**.**

	C_l	C_d	C_m
Reference	0.546/1.371	0.0071/0.0151	0.0798/0.0704
mLEc12	/1.388	/0.0132	/0.0802
mTEc72down	1.133/1.779	0.0124/0.0423	0.1813/0.1543
mTEc72up	-0.250/	0.0063/	-0.0723/

compliant devices was the generation of the background load paths layouts, wich represent a design parameterization of their compliance distribution. In this section, the application of SPHERA to the design of the wind tunnel compliant leading and trailing edge is described, according to the Load Path Representation, coupled with a dedicated Genetic Algorithm, already presented in [17]. One of the main advantages of the load path approach is its intrinsic capability to ensure structural connectivity [28]. The level of parameterization depends on the number of active output points, and the numebr of internal points together with the maximum load path length *maxPathLength*, which is the maximum number of edges included in a path. If the output points placed along the skin are determined by a specific strategy based on the shape optimization results, the designer can choose the value to be assigned to *maxPathLength*. A value equal to 3 or 4 is usally suitable to correctly design any compliant leading and trailing edge device. The level of parameterization determines the initial population size which is set as a multiple of the number of variables: a population size equal to 1 or 2 times the number of variables assures the repeatability of the results in all the examined cases. The load path representation method is coupled with a Parametric Finite Element Model (PFEM) code which incorporates a nonlinear analysis solver, based on an Object–Oriented implementation of the Finite Volume Beam (FVB) elements [29]. The code implementation is derived from the source code of MBDyn software and the validation is based on the same examples [30]. The Finite Volume C0 Beam is a three–node non–linear beam, based on a collocated evaluation of internal forces and moments, usually adopted as deformable connection component in the multibody applications. Each load path can be decomposed into a sequence of Finite Volume Beam connections in order to produce the corresponding finite element model which is used to compute the compliant mechanism deformation.

In order to design a compliant mechanism able to meet both kinematic (motion) and structural (load–carrying) requirements, the design must be decomposed into several parts considering the mechanism design and the structure design, respectively, for a number of load conditions corresponding to the analyzed aerodynamic condition. This is a typical multi–objective design problem that was efficiently incorporated into the Genetic Algorithm [31]. The approach used for solving this kind of problems applied to our purposes is the so called Elitist Non–Dominated Sorting Genetic Algorithm (NSGA–II) [32].

Different kinds of objective function can be considered. The first one is the minimization of the error, in a least square sense, between the deformation of the compliant mechanism once actuated and the optimal target shapes obtained by PHORMA (kinematic requirement). The comparison between the two shapes is done for a discrete number of control points distributed over the airfoil contour. The second one represents the minimization of the least square error between the deformation and the initial undeformed airfoil (structural requirement), when the morphing mechanism is loaded by the external aerodynamic loads and the actuation input point is kept fixed. Each objective function can be associated with a user–defined number of design load conditions, increasing the total number of objective functions. An optional third objective function is related to the minimization of the stress inside the mechanisms. This objective guarantees the capability of the morphing device to sustain the external loads, corresponding to the considered load condition, without excessive deformation.

The multi–objective Genetic Algorithm find multiple optimal solutions represented by a Pareto Front. At the end of the process, the designer selects the design point directly from the Pareto Front, taking into account manufacturing requirements not included in the optimization problem. In the case here described, in order to simplify the optimization problem and to limit the potential size of the design space, the multi–objective optimization problem is formulated as a 2D problem, finding the optimal compliant structure for a selected rib, later extended to the complete 3D space.

The following subsections outline the results obtained from the multi–objective optimization sequence implemented inside SPHERA.

A. Optimal Compliant Leading Edge

The structural definition of the LE compliant ribs was carried out by means of SPHERA, starting from the morphing target shape *mLEc12*, obtained by PHORMA in Section III and characterized by 7 deg droop angle. For a proper execution of the multi–objective genetic algorithm, a combination of two objective functions is considered:

1) Structural requirement: minimizing the least square error between deformation and undeformed airfoil, under the aerodynamic loads corresponding to the undeformed shape, while the morphing mechanism is kept fixed;

2) Kinematic requirement: minimizing the Least Square Error (LSE) between the target morphing LE shape (*mLEc12*) and the deformation computed by PFEM when the mechanism is actuated, under corresponding external aerodynamic loads.

Two different load conditions in terms of angle of attack, both realized at prescribed airflow velocity of $40\,\mathrm{m/s}$, were considered: $\alpha = 2\,\mathrm{deg}$ and $\alpha = 10\,\mathrm{deg}$ for both structural and kinematic requirements.

The leading edge target shape change was obtained without skin length variations, meaning $\sigma_{axial} = 0$. In this way the morphing LE can change its aerodynamic shape in an efficient way, without generating axial stresses. The corresponding leading edge structural model was characterized by two clamps at the upper and lower skin connections with the structural interface points (2 and 3 in Fig. 3), while an horizontal actuation force pushed in the left direction trying to deflect the leading edge downward (point 1). A total of 8 active output points (4 --→ 11), was used for transferring the actuation loads from the inner compliant mechanism to the outer skin. Additional deactivated points were also introduced along the leading edge contour in order to improve the resolution of the results and better distribute the external loads. The C_p distribution computed around the airfoil is transferred, in terms of lumped forces, to the grid points placed along the skin structural model by an interpolation technique based on the same CST formulation adopted for the parametric geometry representation. Figure 3 shows the two different load conditions coming from the aerodynamic computations and transferred to the structural grid points. A total of 9 separate regions along the leading edge boundary, where thicknesses vary interdependently in the course of the optimization process, were used. Moreover 5 internal points (23 --→ 27), were collocated in the user–defined airfoil domain to define the initial population of load paths. During the optimization, the load path cross–sectional thickness was free to vary between $1\,\mathrm{mm}$, and $7\,\mathrm{mm}$.
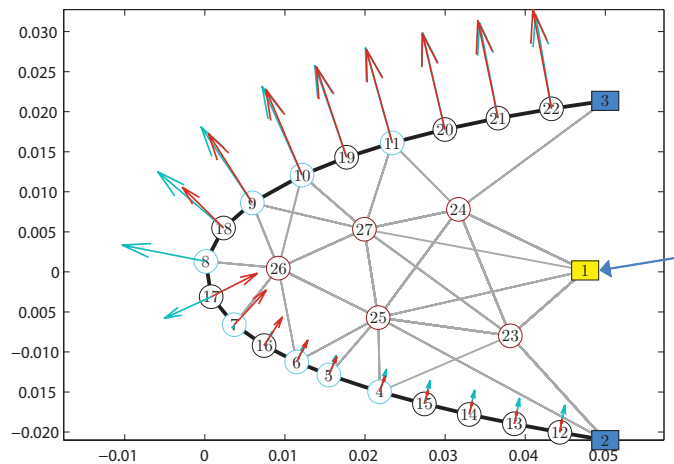
Figure 3   Multiple aerodynamic loads applied to the initial load path model of the compliant leading edge and corresponding characteristic points

In this design case the stress constraint along the skin, considered during the shape optimization 1 as maximum curvature difference, is not included. The genetic algorithm accounted an initial population of 300 individuals and was left free to run for 700 generations. After 420 iterations a Pareto Front was invoked, which made easier to identify the best design trade–off between kinematics and structural objectives in terms of LSE deviations. Figure 4 (right) shows Pareto front solutions obtained for the previously introduced leading

13

edge and the selected design point. In particular the point highlighted with red color represents the best compromise between the two objectives and shows a LSE value of 4.15×10^{-4} m, concerning the kinematic requirement.

The required deformation behavior led to a total requested actuator stroke for the complete airfoil morphing equal to -5.1 mm, along the vertical direction and -2 mm, horizontally. Figure 4 (left) shows the compliant mechanism and the corresponding deformation.
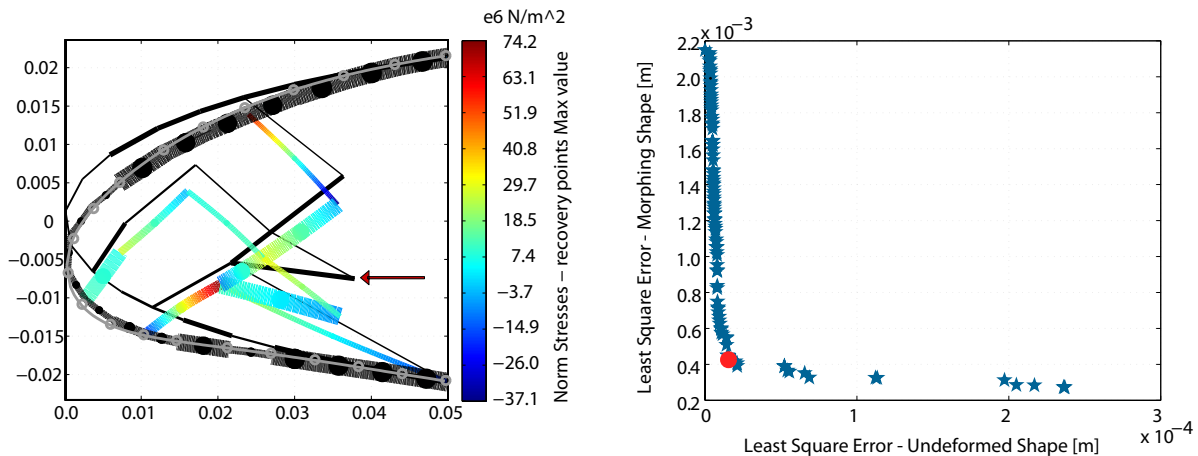

Figure 4   The final structural configuration (left) and the Pareto Front (right) related to the LE optimization

The stress values, computed inside the compliant structure and shown in Fig. 4, never exceed the corresponding flexural strength of Table 1 until the actuator stroke, required to reach the target shape deflection, is introduced.

B. Optimal Compliant Trailing Edge

In the case of TE a similar procedure was followed. The main differences with the LE case are due to the special requirement of a two–directional deflection during morphing, i.e. the upward and downward movement of the external airfoil skin. Even in this case a multi–objective optimization was carried out, tailoring analogous kinematic and structural requirements, this time differentiated in both up and down configurations for the two separate airload conditions of Table 2, at 40 m/s of flow velocity. The design requirements are:

1) Structural requirement: minimizing the least square error between deformation and initial undeformed airfoil, under the aerodynamic loads corresponding to the undeformed shape, when the morphing mechanism is kept fixed;

2) Downward kinematic requirement: target shapes labeled *mTEc72down* in Section III, under corre-

14

sponding external aerodynamic loads;

3) Upward kinematic requirement: target shapes labeled $mTEc72up$ in Section III, under corresponding external aerodynamic loads.

Compared to the leading edge, the trailing edge model has a different compliant architecture, much more flexible due to the totally distinct kinematic capabilities. Indeed, the two TE interface nodes are split into antithetical boundary conditions: the upper skin connection node is fixed (point 2 in Fig. 5), while the lower skin node is free to move along lower skin contour, with a direction tangent to the local curvature of the airfoil (point 1). This peculiarity offers the possibility of a push–pull actuation system, according to the need for two–directional morphing shapes and it is implemented in the load path model through a slider which is constrained or free to rotate. During the shape optimization run the lower skin length constraint was relaxed because the target shape embeds this effect. A total of 8 active output points, 4 on the upper skin arc (3 --→ 6) and 4 on the lower one (7 --→ 10), was used for transferring the actuation loads from the inner compliant mechanism to the outer skin. A total of corresponding 11 separate beam segments, where the skin can vary independently, were used: 5 along the upper skin, 6 along the lower one and 1 flexible small connecting brace in the proximity of the cusp are shown in Fig. 5. Moreover 6 internal points (21 --→ 26), were collocated in the user–defined airfoil domain to define the initial population of load paths. During the optimization process, the load paths cross–sectional thickness is free to vary between 1 mm, and 4 mm.
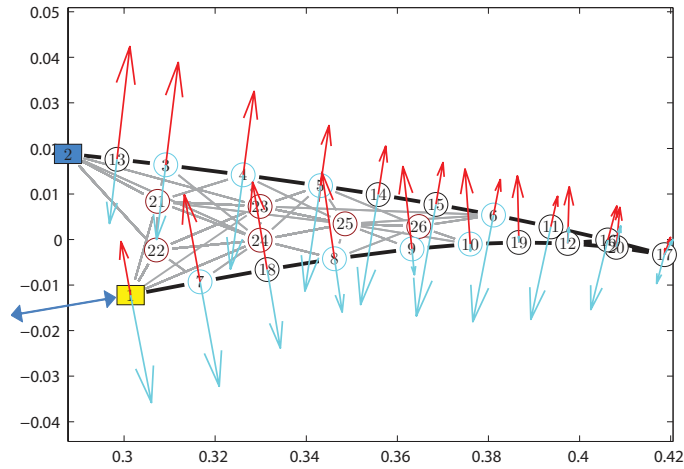
Figure 5 Multiple aerodynamic loads applied to the initial load path model of the compliant trailing edge and corresponding characteristic points

This time the optimization algorithm started from an original population of 200 individuals, limited to 500 generations in the growing phase. After 360 iterations, the Pareto Front shown in Fig. 6, represented by a three–dimensional surface, was obtained. Due to the need for guaranteeing an adequate deformation performance in both up and down directions, it was necessary to pursue a balanced LSE. A dedicated

The final outcome is the red–marked point, characterized by LSE values of 0.57×10^{-3} m, and 5.2×10^{-3} m, respectively for downward and upward deflections. The LSE related to the structrual requirement (undeformed shape) is 2.0×10^{-4} m. This solution represents a single–piece adaptive rib with a span-wise thickness of 1.5 mm.
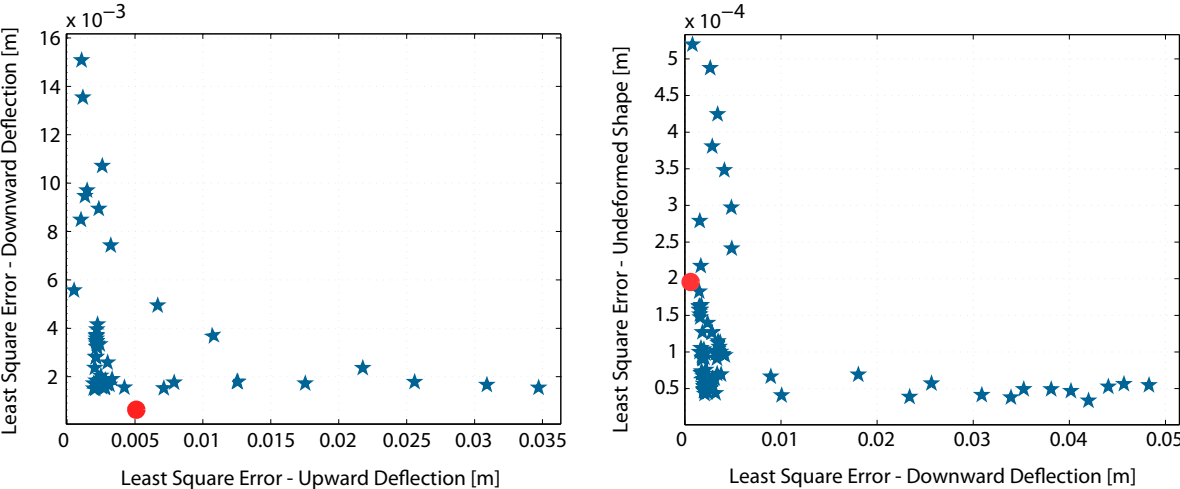

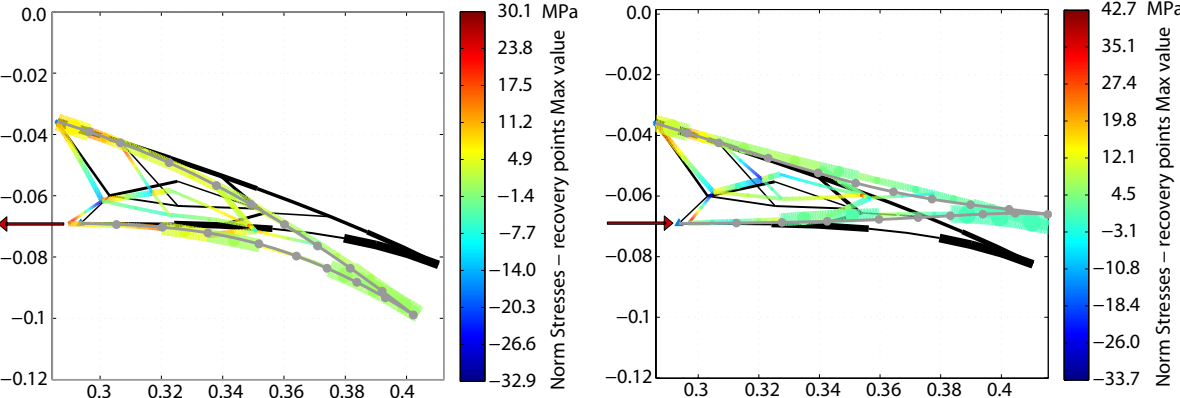**Figure 6   The Pareto Front related to the TE optimization.**

Figure 7   The final structural configuration for downward (left) and upward (right) deflection of the morphing TE.

The design model has been extracted from the Pareto Front. Figure 7 shows the corresponding optimal

16

compliant structure of morphing trailing edge, in both maximum downward and upward configurations. The requested actuator stroke to meet the two kinematic requirements, are equal to $-4\,\mathrm{mm}$ for the downward deflection and $2\,\mathrm{mm}$ for the upward deflection, applied to the lower skin in the direction parallel to the skin. These values agree with the $\Delta L_{TE,LowerSkin}$ constraint used in the shape optimization 2 and confirm the correlation between PHORMA and SPHERA. The resulting trailing edge configuration keeps a low level of axial stresses and does not suffer from instability problems. Indeed, the main difference in terms of structural behavior between the LE and the TE is that the last one is not clamped to the rear spar in both sides, upper and lower. This is the case where typically the buckling appears on TE when you try to morph it. In our case, the lower skin of the TE is free to slide, since this is the actuation mechanism implemented, so avoiding any skin buckling problem. This behavior has been easily identified during the design process. In both cases, downward and upward configurations, the normal stress (combination of axial and bending stress) field inside the mechanism are lower than the material flexural strength limit of $78\,\mathrm{MPa}$.

V. 3D Modelling of the Optimal Compliant Leading and Trailing Edge

The post–processing of the compliant LE and TE, designed as 2D FEM models, was required for three main reasons: generate 3D Finite Element Models (FEM) directly from the Pareto Front results in order to validate the structural behaviour of the morphing skin estimated during the shape optimization; perform analyses on detailed Finite Element Models in order to check the local stress concentrations and compare the wind tunnel test results; generate CAD models to manufacture the compliant leading and trailing edge devices by means of Stereolithography (SLA) or Selective Laser Sintering (SLS) techniques. The link between SPHERA and PHORMA allows to quickly generate different CAD and FEM models, starting from the same optimal compliant solution coming from the two–level design procedure. Corresponding CAD models, described in Section B and based on the optimal topological solution, have been used both to perform adaptive meshing for the stress level validation and to manufacture corresponding 3D print prototype.

A. Finite Element Analyses

Different 3D models, composed by several ribs and few actuation points, have been generated in order to check the morphing structural response. Both full 3D adaptive mesh (solid elements for the rib connected to plate elements for the skin) and hybrid mesh (two–node beams for the compliant mechanisms connected to four–node plate elements for the skin) have been adopted for validation. Full mesh is used for the accurate stress evaluation inside the compliant mechanism, while hybrid mesh can be automatically generated by PHORMA and it is suitable for sizing 3D structural components and for the skin stress evaluation. Corresponding analyses are performed using the non–linear static solver of MSC/Nastran software and only results coming

Finite element analyses allowed to introduce and design 3D structural components that are not included in the load paths models. In the case of compliant leading or trailing edge devices, this allows to optimize the final design with respect some parameters, such as the number of ribs, the size and orientation of the stringer or different actuation systems. In particular, the 3D model of the leading edge has been realized connecting to the skin a total of 9 equally spaced compliant ribs, with span–wise thickness of 10 mm. The same strategy has been adopted to calculate the 3D skin thicknesses, starting from the values obtained by the genetic algorithm. In order to distribute in the span wise direction the morphing deformations introduced by each compliant leading edge ribs, 3 stringers, placed where the load paths are attached to the skin, have been introduced in the compliant leading edge device.

A new strategy based on a high number of compliant ribs but with a limited number of actuators has been adopted for the trailing edge. The compliant trailing edge design led to a solution where no stringers are expected. It is actuated by only two linear actuator at the span wise ends of the surface. The actuation forces are introduced in a plane parallel to the lower skin that is left free to slide along both the airfoil surfaces and the span. In this way it is possible to uniformly spread the actuation stroke along the span so that each rib achieves the requested actuator stroke coming from the optimization.
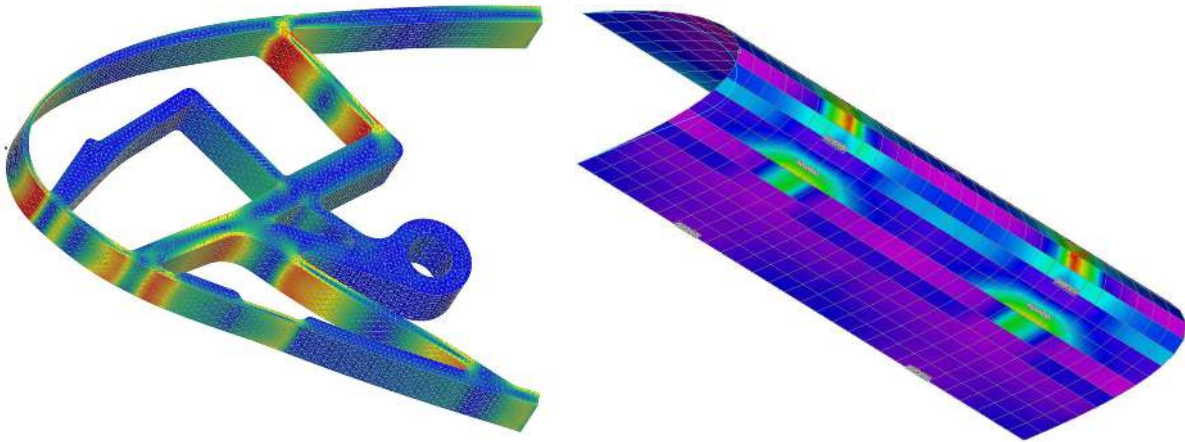

Figure 8   Finite element models used for the morphing LE verification.

This design phase allowed to validate the compliant mechanism synthesis procedure, confirming all the simulations performed during the Genetic Algorithm (GA) computation on the 2D reduced–order models. Deformation and stress distributions computed along the hybrid and the adaptive full models are reported in Fig. 8 and agree with the 2D structural results obtained during the shape optimization and by the PFEM code. Concerning the hybrid models, mesh convergence studies led to the definition of finer mesh than those

adopted by PFEM. In order to guarantee the convergence of the non–linear analyses, 15 load steps and a maximum of 40 iterations, with $1.e-5$ of tolerance, were adopted. The 3D results of leading and trailing edge were compared with the deformation shape and the stress distribution obtained during the whole design process. On the one hand, the optimal morphing shape and the stress field, estimated along the skin by the CST parameterization method, were validated by the results obtained on the hybrid model. On the other hand, the full model was used to validate the results, in terms of internal structure stresses, provided by the PFEM and shown in Fig. 4 and 7. In the first case, the errors between FEM deformations and target shapes are very close to the LSEs obtained from the Pareto fronts, while the maximum stress value computed along the skin of the hybrid model is about the 8% (leading edge) and the 5% (trailing edge) higher than that estimated by the shape parameterization. In the second case, the internal stress values computed into the full model and those computed by PFEM are very similar.

The deformation shapes obtained from the 3D hybrid model analyses were used to perform two additional RANS computations in order to compare the aerodynamic performances with those provided by the optimal target shapes. The CST parametric identification described in [18] was applied to the FEM displacements and the same kind of structured D–meshes described in section III were automatically produced. Due to the small values of LSEs coming from the kinematic requirements of the multi–objective optimization, the aerodynamic analyses performed on the deformation shapes provided the same results reported in Table 2.

B. Generation of the CAD Models

The framework is equipped with an interface able to export the solid model of the compliant device in the most common CAD formats, such as IGES and STEP, as well as CATIA$^{©}$ files. An initial CAD model is exported considering the internal points position, the internal load paths thickness and the skin thickness distribution of the compliant solution as parametric quantities.

The same procedure is able to introduce additional parametrical parts, such as stringers, the connection zones between wing box and morphing skin and the actuator connection, after checking them using the 3D FEM models. This assists the engineers in the design of the final compliant device. Figure 9 shows the CAD models of the leading and trailing edge devices, after designer intervention.

The complete morphing leading and trailing edge were manufactured in a single piece, directly starting from the CAD model, as sketched in Fig. 9. At the end, the SLA and SLS techniques have been adopted to print the morphing devices prototypes.
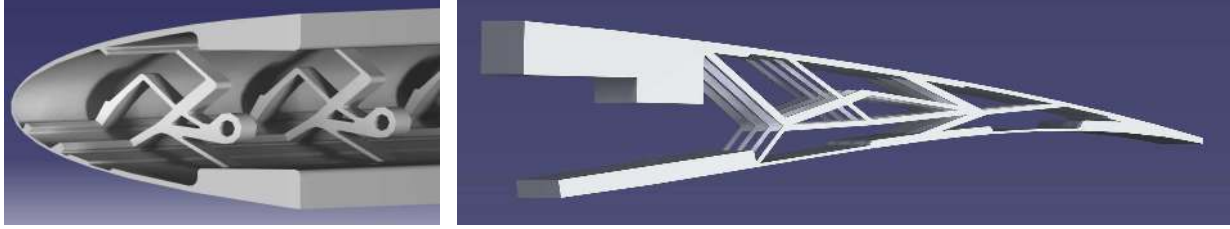
Figure 9   Leading and trailing edge CAD models ready for 3D printing manufacturing.

VI. The Wind Tunnel Model

The wing model is mainly composed by a wing–box acting as a rigid support for the morphing LE and TE and accommodating the measuring devices and actuators. The wing–box is constituted by different structural components that are shown in Fig. 10, where the wing model is assembled without the morphing devices. The front and rear spars were obtained by milling two solid blocks of Aluminum Alloy 6082. Both of them have a symmetric T shaped cross section, which enables the attachment of morphing LE and TE through a series of threaded joints. Two end plates, located at both wing tips, are used to support the spars and to ensure fastening to the test rig in the wind tunnel. Six ribs are connected to both spar members by bolts. Each rib is provided with a central hole hosting the measurement systems and wiring. The ribs also host the actuation system by means of the seats for the bearings that support the camshaft. The camshaft allows to impose the linear movement to the connecting rods pushing or pulling the LE. This type of mechanism assures accurate displacements and rotations, and also has not restrictive limitations in terms of the amount of transferred loads. This solution has been adopted for the preliminary test in place of more sophisticated systems based on electrical servo–actuators. Two transparent skin panels, made of Polyethylene Terephthalate panel with a thickness equal to $1.5\,\mathrm{mm}$, are chosen to be able to guarantee an aerodynamic shape and at the same time allowing to inspect the internal wing during the test campaign.

The wing model has been designed to be rigid, for sure in the range of the wind tunnel speed here investigated. The main reason for that was to avoid any aeroelastic influence on the obtained morphing shapes, both with and without aerodynamic loads. Aiming at this goal, the structural elements of the wing have been oversized, and the wing model is clamped in both sides to the vertical frames of the wind tunnel. In this way, the measured morphing shapes depend only on the compliant structures implemented for LE and TE and their possible deformation under the effect of the aerodynamic loads, but they do not depend on the deformation of the wingbox.

The manufacturing of compliant structures at a small scale represents a challenging target due to the strict accuracy requirement to correctly reproduce the stiffness distribution. The 3D printing technology has been identified as a potential candidate to realize the morphing devices in a single piece with the requested
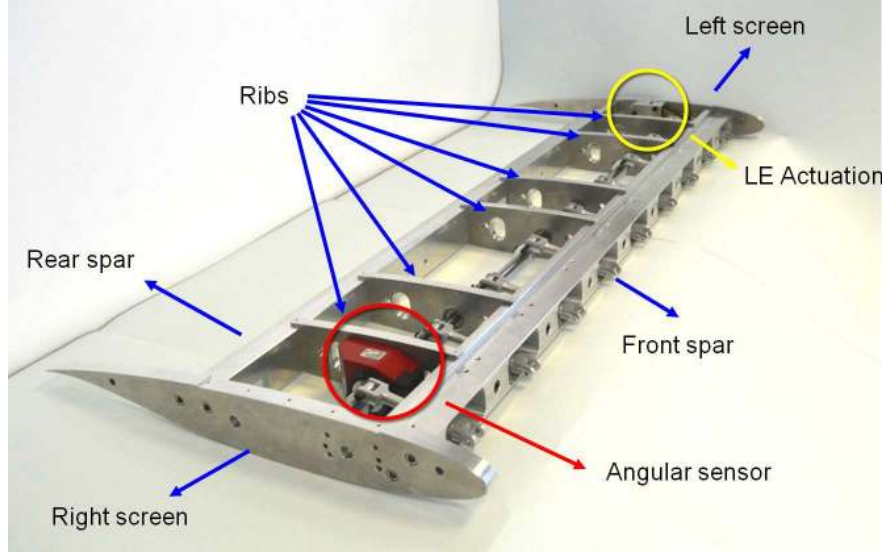
20

Figure 10   A sketch of the wing model without the morphing LE and TE.

accuracy in terms of thickness distribution (of the order of magnitude of 0.5 mm). For this reason, a series of prototypes have been realized to identify the best 3D printing technique and the most suitable material, at the end identified as the SLA using *Somos GP Plus 14122* and the SLS using *PA 2200.*

Since the main goal of the preliminary test campaign is the validation of the numerical models adopted for the design of the compliant mechanisms, the following quantities are considered in the design of the measurement system: the deformed shape of the morphing devices to be compared with the predicted ones, the actuation forces and the pressure distribution. The adopted measurement systems are then based on a load cell connected to the rod actuating the morphing LE, and an angular sensor to measure the droop angle of the LE, pressure taps located on the central part of the model. Concerning the measurement of the deformed shape, it is based on photogrammetric techniques as explained in the following section. Figure 11 shows the two sensors installed into the wing to measure the input actuation in terms of rotation of the camshaft, which drives the leading edge, and force introduced into each rib; Figure 12 shows morphing leading and trailing edge in their deformed configurations, adopted during the wind tunnel tests.

VII. Experimental Tests

The Sergio De Ponte wind tunnel at POLIMI is shown in Fig. 13 together with the oscillating system used for the precision positioning of the morphing wing model in terms of angle of attack [33]. As already mentioned, the morphing wing model has a span of 930 mm and a chord of 418 mm.

The wind tunnel tests were performed at 40 m/s, in the range of angles of attack between 0 deg and 17 deg, considering four different wing shape configurations corresponding to the undeformed airfoil, the morphing
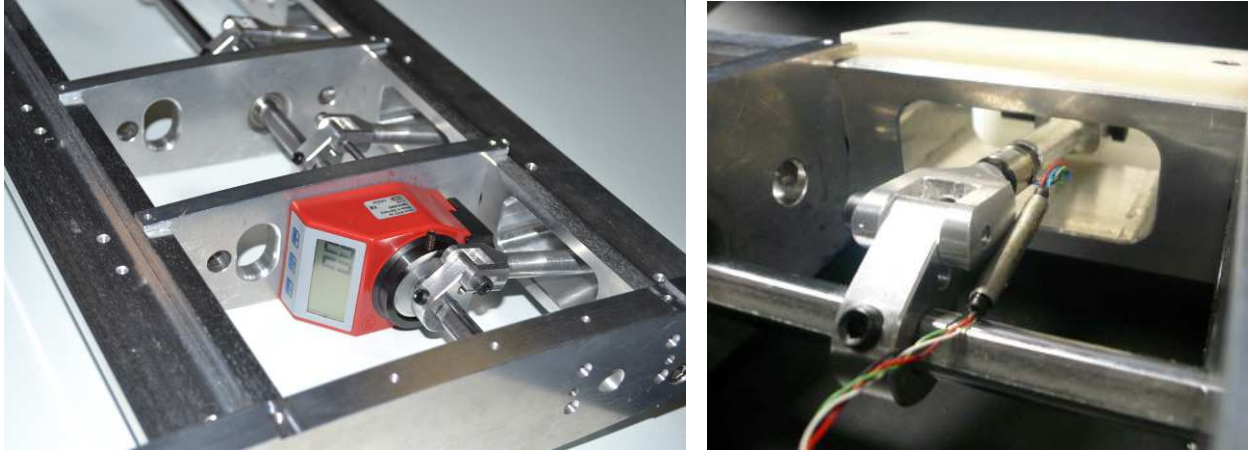
21

Figure 11   The LE angular rotation sensor (left) and the load cell for actuation load measurement (right).

Figure 12   A sketch of the wing model with the assembled morphing LE and TE.
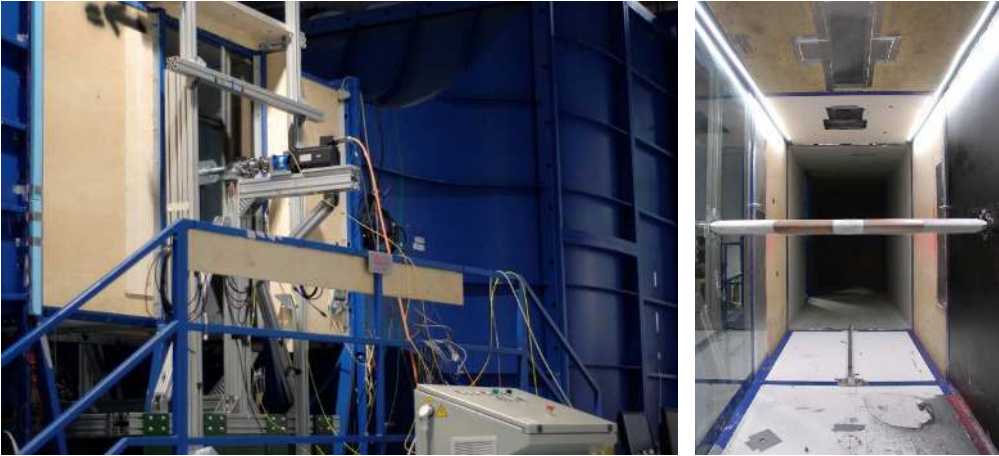

Figure 13   An overview of the Sergio De Ponte wind tunnel equipped with the oscillating test rig and the morphing wing model in the test chamber at PoliMi.

leading edge, the morphing trailing edge and the combination of morphing leading and trailing edge. In all cases the morphing leading and trailing edge configurations are related to the morphing shapes labeled *mLEc12* and *mTEc72down* in Section III. During the tests, the test chamber temperature ranged from 15.79 °C to 17.79 °C (average temperature 16.71 °C), while the absolute environmental pressure ranged from 98 731 Pa to 99 451 Pa (average pressure 98 994 Pa). The air density had an average value of 1.18 kg/m^3. Two wind tunnel testing campaigns, described in the next sections, were conducted.

A. Morphing shape validation

The first tests were conducted to validate the capability of the morphing structures to reach the target shapes. The measurement of the morphing shapes on a wing is still an open issue, especially for flight test but also for wind tunnel test. In some cases, for wind tunnel tests, dedicated, and very expensive, laser scanning instruments can be adopted. For this reason, the photogrammetry-based systems are very interesting. Two kind of approaches can be adopted: the one based on infrared camera able to track specific markers installed on the model or the second one based on full field measurement that is able to reconstruct the complete geometry by Digital Images Correlation (DIC) methods on the basis of pictures of the specimen previously jeopardized with high contrast colors. In DIC methods the known position of the cameras as well a calibration and a correction process is requested.

In order to capture the morphing shape obtained during the experimental tests, the Close–Range Photogrammetry, also called Image–Based Modeling, was adopted, as implemented in the photogrammetry software named ReCap$^{\text{TM}}$. The main advantage of this approach is that it does not require any calibration process and is able to reconstruct the full 3D geometry of the subject on the basis of a high number of pictures, at least 16–18, taken around the subject from different, while unknown, positions and orientations. The software is able to recognize the details of the subject and reconstruct its complete 3D geometry. In our case we used 24 images taken with a single camera Nikon D80 camera of 10.2M pixel of resolution hand–held and placed close to the wing model. The calibration process has been automatically carried out by comparing the original 3D shape of the wingbox, as available in CATIA$^{\copyright}$, to one reconstructed by the software: the two resulted perfectly overlapped. Based on these considerations, the accuracy of the system adopted to reconstruct the morphing shape can be considered of the order of sub-millimeters, believed enough for the considered experiment.

The output of the software is a 3D model in the form of point clouds, as STL file. By means of the Digitized Shape Editor workbench inside CATIA$^{\copyright}$, the STL model was interpolated and converted into the corresponding analytical CAD model, used to extract a selected wing cross–section shape. Figure 14 represents the STL model obtained by ReCap$^{\text{TM}}$after the same actuator stroke required by the FEM analyses

was used to deform the wind tunnel model.

The deformed curves, corresponding to the selected cross–section and shown in Fig. 15, have been used to evaluate the numerical/experimental correlation, defined as the LSEs between the optimal target shapes, obtained from the shape design, and the wind tunnel model deformations. The comparison between the leading edge downward deflections provided a LSE of 3.71×10^{-4} m, while the comparison between the trailing edge downward deflections provided a LSE of 0.8×10^{-3} m, which indicates that the two deformations are very similar. These values are very close to the same LSEs extracted fromt the Pareto fronts and allows to experimentally validate the design method and the results obtained by SPHERA.
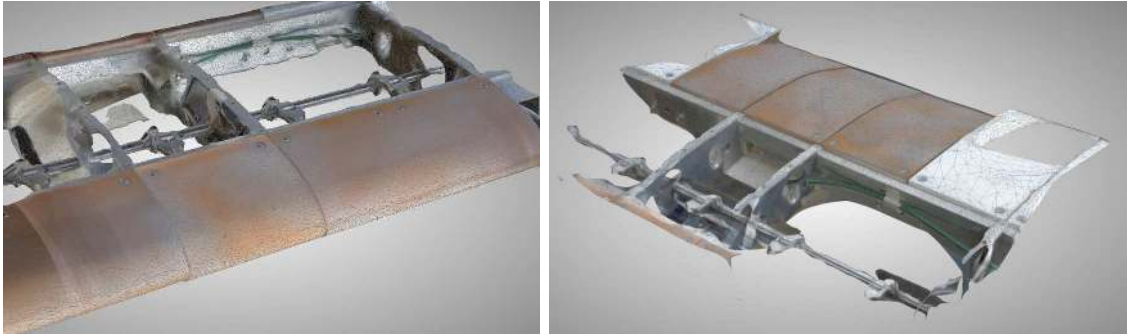
Figure 14 The digitalized images of the deformed morphing devices used for image correlation.
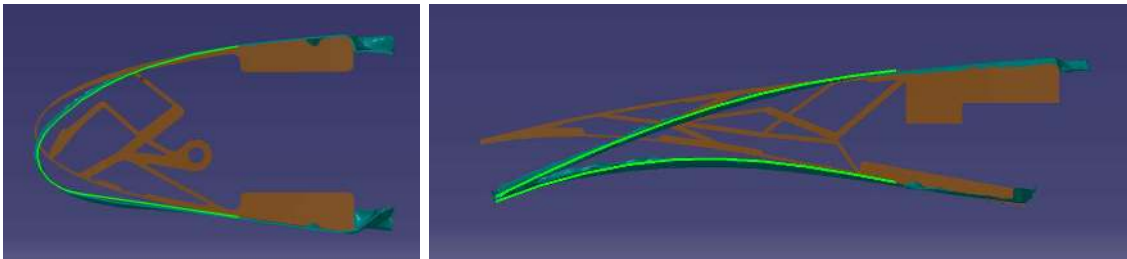
Figure 15 The identified deformed shapes (dark green) compared with the optimal (target) ones (light green).

During this experimental campaign, the compliant devices have shown to be able to perform the task required for a morphing control surface that, as introduced in [18], must be a flexible structure able to adapt its shape as expected and, at the same time, an enough rigid structure able to maintain its shape under the aerodynamic loads, when the morphing mechanism is not actuated.

B. Aerodynamic assessment

The second wind tunnel testing campaign was conducted to:

- validate the CFD computations performed on the optimal morphing shapes obtained by PHORMA;

- trace the experimental $C_l(\alpha)$ curve to define the potential performance benefits of morphing technologies.

For this purpose the tests were conducted at the fixed wind tunnel speed of $40\,\text{m/s}$, but spanning a wider range of angles of attack. Actually, the speed was reduced to $30\,\text{m/s}$, beyond $15\,\text{deg}$, for security issues but the Reynolds number change due to the different speed didn't affect the dynamic pressure. Moreover the C_p curves remained smooth. Indeed, the first campaign allowed to grasp the model behavior in the linear part of the $C_l(\alpha)$, while in the second campaign it was possible to study the region near (and beyond) the stall. Thus, the angle increment, from $0\,\text{deg}$ to $10\,\text{deg}$, was $2\,\text{deg}$, while it was refined to $1\,\text{deg}$ beyond $10\,\text{deg}$. The maximum angles reached for undeformed, leading edge deflected, trailing edge deflected and leading edge combined with trailing edge, were $17\,\text{deg}$, $21\,\text{deg}$, $17\,\text{deg}$, and $18\,\text{deg}$, respectively. The middle section of the model, where a two-dimensional flow is likely to occur, is equipped with pressure taps: in particular the leading and trailing edge central sectors were directly 3D–printed with the holes and housing for the tubes, while the upper and lower wing–box skin, made of Polyethylene Terephthalate, were drilled and the tubes attached with glue.
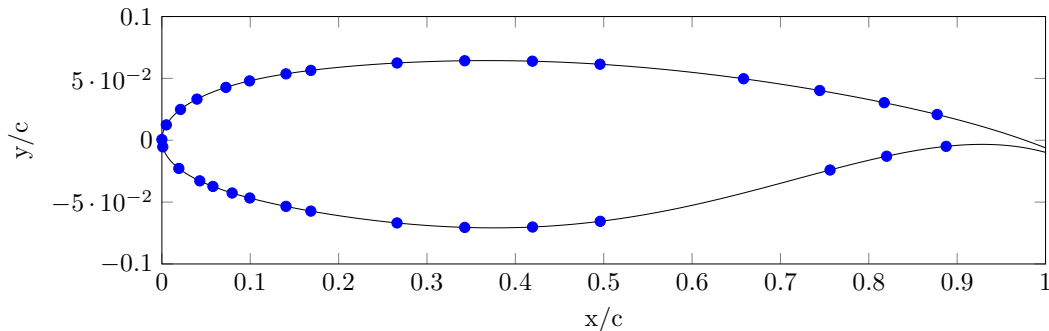
Figure 16   Pressure taps locations on the reference airfoil shape

The total number of pressure taps is 31: 16 on the upper skin and 15 on the lower skin (see Fig. 16 for a schematic representation). As can be seen in Fig. 17, the taps are offset in the span–wise direction to avoid mutual interference and to allow tubes storage, in particular for the leading edge; since the flow is expected to be uniform in the central part, the staggered pattern doesn't affect the measurements. The rearmost pressure tap is located at about 90% of the chord since it wasn't possible to go any further due to the allowable space in the trailing edge.

A 32–channel miniature Esterline electronic pressure scanner coupled with a DTC Initium DAQ system – global accuracy $0.06\,\%$ of full scale ($7\,\text{kPa}$) – is used to acquire the pressure taps; each channel is sampled
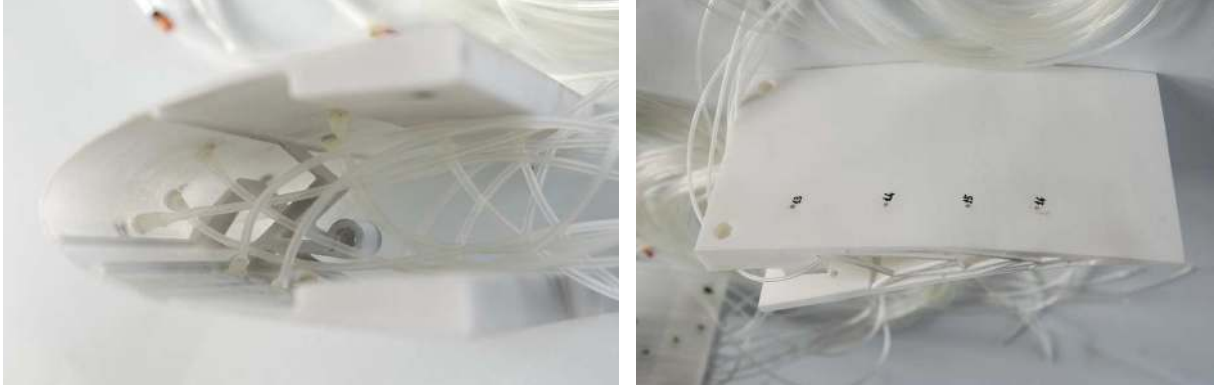
Figure 17   Details of pressure taps and tubes: leading edge (left) and trailing edge (right)

at $100\,\mathrm{Hz}$ for $10\,\mathrm{s}$ and only the average value of the pressure time history is saved, given the nature of the static tests.

The pressure coefficient distributions for the two conditions used in the design of the compliant mechanism are presented in Fig. 18. The leading edge droop "shifts" the suction peak towards the trailing edge, thus moving the "center of gravity" of the C_p area backwards and changing the pitching moment, while the trailing edge deflection increases the maximum value of the peak and the area of the curve, increasing the lift force generated; the combined effect of the two morphing surfaces globally enhances the aerodynamic performance with respect the reference shape. The same behavior is found at an angle of attack of $10\,\mathrm{deg}$ even though the effect of the leading edge is less noticeable due to the combination of high incidence and high speed.
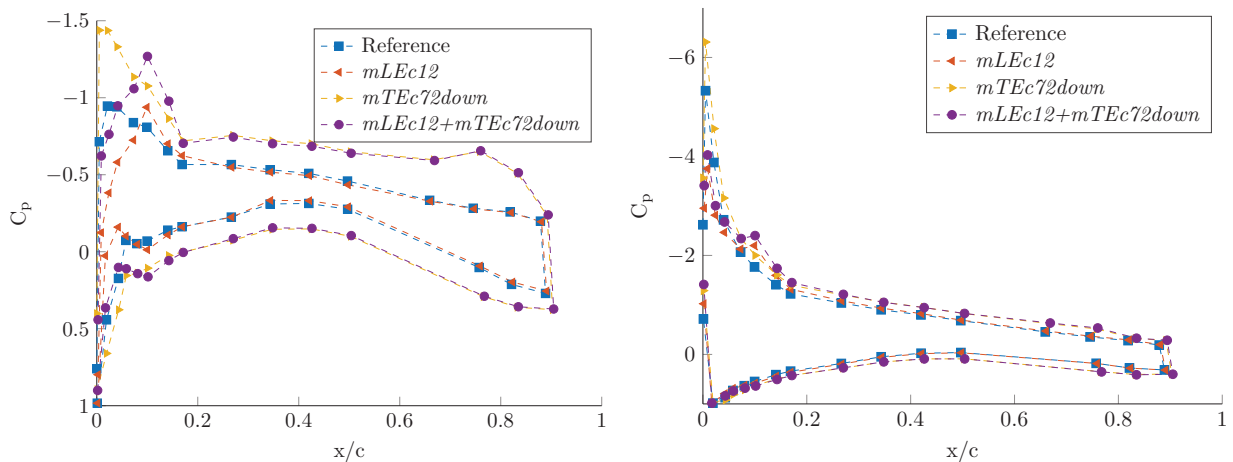
Figure 18   Experimental C_p distribution for $\alpha = 2\,\mathrm{deg}$ (left) and $\alpha = 10\,\mathrm{deg}$ (right), respectively, corresponding to a wind tunnel speed of $40\,\mathrm{m/s}$

The aerodynamic analyses used to compare with the experimental results are the same RANS simulations already used in the shape optimization. In order to validate the aerodynamic loads used by PHORMA, CFD

Since the original loads came from an isolated wing in free stream, a fair comparison between results should rely on an effective angle of attack, α_e. In the wind tunnel the model experiences a different induced angle due to the presence of the walls and three–dimensional effects due to the finite aspect ratio. This effect is taken into account using a linear correction law for the angle of attack, deduced by the comparison of the experimental $C_l(\alpha)$ curve with the CFD one's, the latter obtained integrating on the same points (i.e. the 31 pressure taps locations): when the angle of attack approaches high values, the blockage effect is stronger causing a greater induced angle and increasing the gap between the two $C_l(\alpha)$ curves (the maximum blockage effect is about 9% at the maximum tested angle of attack of 21 deg). Keeping constant the C_l value for a given (experimental) angle of attack, it's possible to identify the corresponding point onto the CFD $C_l(\alpha)$ curve, thus a new analysis is run at the corresponding effective angle of attack. The comparison between experimental measurements and computed values for the reference configuration is shown in Fig. 19 where the C_p distributions appear in good agreement at 2 deg and perfectly match at 10 deg.
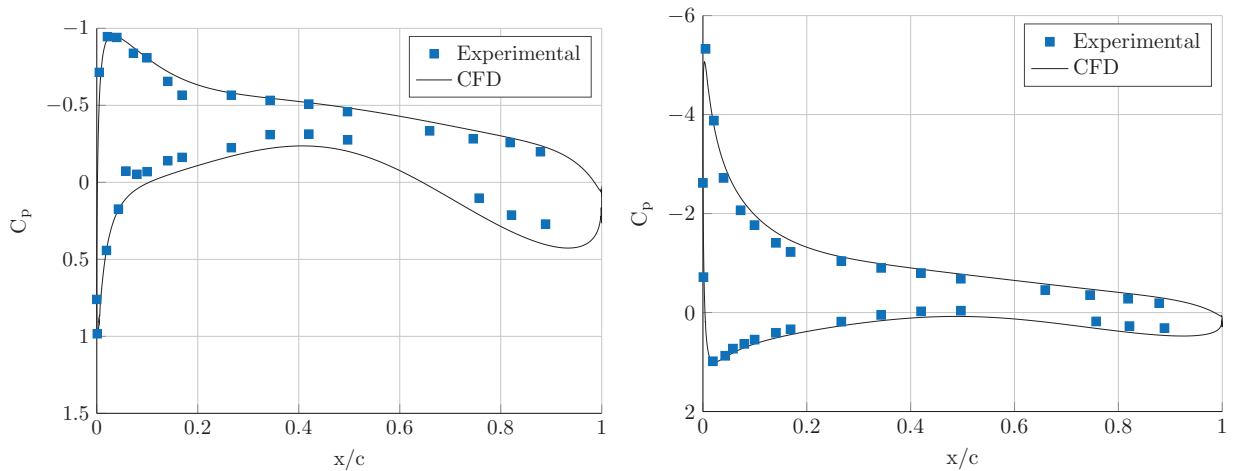
Figure 19   Comparison between CFD analyses and wind tunnel C_p distributions around the reference wing, for $\alpha_e = 2\,$deg (left) and $\alpha_e = 10\,$deg (right)

The same procedure is thus applied to the *mLEc12* and *mTEc72down* morphing configurations. The comparison between the CFD and the experiment related to the deformed leading edge, is reported in Fig. 20. A good agreement is found and this suggests that the CFD predictions could be extended to the drag coefficient of the morphing leading edge concept. It was shown that deploying the leading edge morphing surface alone doesn't produce a noticeable change in the lift curve, but it may improve performances in terms of C_d (at equal C_l) as can
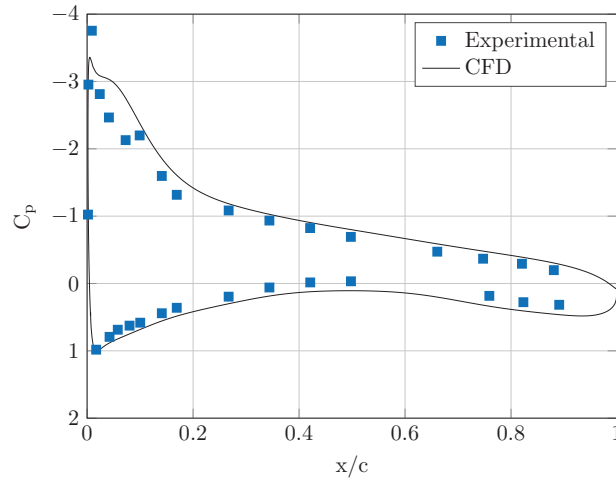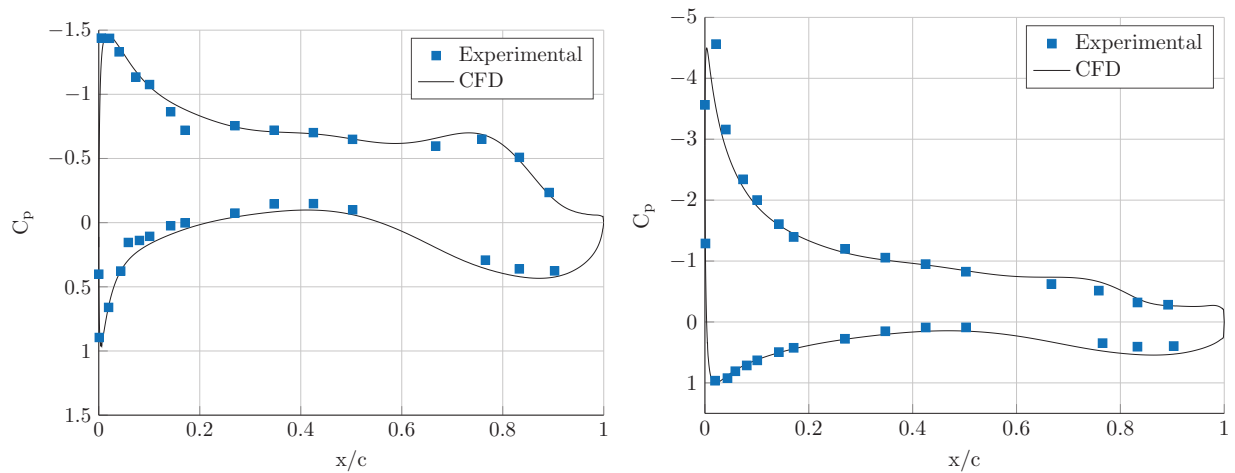
be inferred by Table 2.

Figure 20   Comparison between CFD analyses and wind tunnel C_p distributions around the morphing wing with deformed LE, for $\alpha_e = 10 \deg$

The comparison between the CFD results and the wind tunnel measurements related to the deformed trailing edge at 2 deg and 10 deg, is shown in Fig. 21. Even in this case the CFD results reproduce very well the behavior of the measured pressure distribution. In particular at 2 deg it can be noted that both the CFD and the experimental results show the presence of a bubble between 60 % and 80 % of the airfoil chord.

Figure 21   Comparison between CFD analyses and wind tunnel C_p distributions around the morphing wing with deformed TE, for $\alpha_e = 2 \deg$ (left) and $\alpha_e = 10 \deg$ (right)

The good agreement between CFD pressure distributions and the experimental ones, validates the effectiveness of the geometry representation method embedded in PHORMA and its CFD tool for the evaluation of the aerodynamic loads, representing the main goal of the numerical activity. The actual measurement

The pressure taps locations change due to the deformation of the morphing surfaces, and the new coordinates – needed for the integration of the pressure distributions – are computed on the assumptions that the leading and trailing edges deform keeping constant the arc length (design constraint), and thus the integration was done on the updated coordinates even though only a slight variation in the lift coefficient curves, with respect the same measurement using the reference positions, was noted (see Fig. 22).
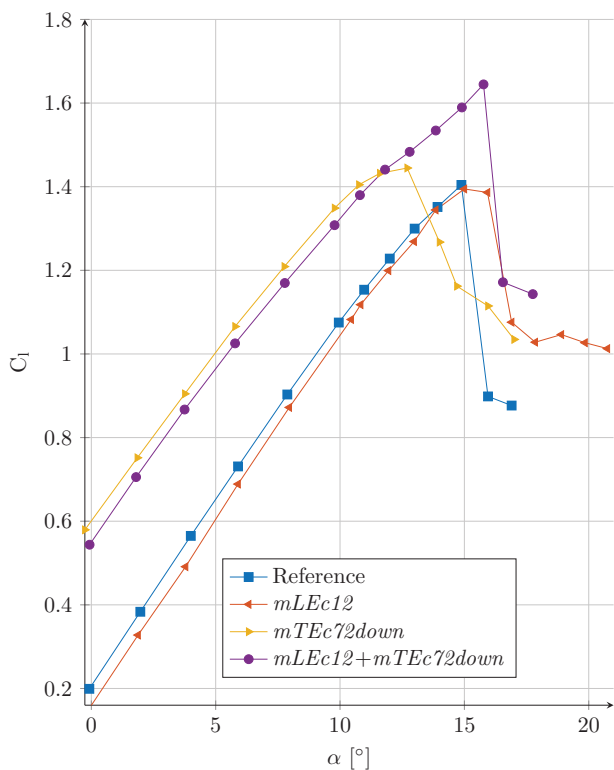

Figure 22 **Experimental $C_l(\alpha)$ curves related to the four configurations: undeformed, deformed leading edge, deformed trailing edge and deformed leading edge plus trailing edge**

As pointed out before, the leading edge causes a "downward" shift of the C_l curve – well known in literature for the leading edge classical control surface – but in return it delays the stall of about 1 deg and still up to 20 deg the C_l value is greater than unity while the reference configuration exhibits a sudden drop below the unity after 15 deg (smoother stall behavior). On the other hand the effect of the morphing trailing edge is to increase the lift, "upward" shift of the curve. The combination of the two devices gives the best performances, leading to a maximum C_l of about 1.64 (1.4 for the reference) with a stall angle of about

16 deg. Even though the leading edge stall–smoothing effect is decreased, after the stall the lift coefficient values remain around 1.1–1.2. From the lift coefficient point of view, the leading edge provides the greatest benefit in terms of stall delay when it is combined with the trailing edge.

VIII. Conclusions

This paper describes the experimental validation of the framework, based on PHORMA and SPHERA tools, developed during recent years at POLIMI for the design of morphing wings. The framework has been used intensively during different EU funded research projects. In particular, it was adopted during FP7-NOVEMOR project to design the morphing LE and TE to be applied to the so-called Reference Aircraft, a regional aircraft developed inside the project by EMBRAER and used for the final assessment of different morphing solutions. A dedicated experiment including the manufacturing of a small scale morphing wing for wind tunnel testing and the design of the compliant leading and trailing edge has been conducted. Finally, the wind tunnel experiment has been designed and carried out to validate the configuration of the proposed morphing devices obtained using the dedicated numerical framework. The adopted tools have been shown to be highly useful design aids, while manufacturing and preliminary experimental testing of the resulting designs have been presented. The first experimental test campaign was devoted to assess the actual morphing shape: a good accuracy between the predicted morphing shapes and the ones actually measured with the photogrammetry technique proved the effectiveness of topology optimization methods for the design of morphing structures. The second experimental test campaign was devoted to the aerodynamic assessment: on the one hand tracing the experimental $C_l(\alpha)$ curves proved the potential benefits of the leading/trailing edge morphing control surfaces, on the other hand the aerodynamic loads used in the compliant mechanism synthesis were validated with the experiment, ideally closing the design cycle. A future programmed improvement is to use a PIV technique to map the flow around the airfoil at different angles and morphing device deflection, gaining a deeper insight in the nature of the phenomenon. During this test campaign the test setup, based on the same oscillating system described in this manuscript, could be equipped with a dedicated load cell, for the total drag measurement, that needs to be appropriately calibrated to cope with the over–costrained nature of the attachment system.

The effect of aeroelastic deformations on the performance of morphing devices represent one of the most challenging aspect. However, this aspect was not investigated in this work due to the preliminary design assumption to use a rigid wind tunnel model, to limit our investigation to the morphing devices and to their validation with respect to the predicted results. The impact of aeroelasticity will be deeply analyzed in a second phase of this research, when the morphing devices will be implemented in the numerical model representative of the full scale reference aircraft.

Acknowledgments

References

[1] Monner, H. P., "Realization of an Optimized Wing Camber by using Formvariable Flap Structures," *Aerospace Science Technology*, Vol. 5, 2001, pp. 445–455.

[2] Hetrick, J. A., and Kota, S., "An Energy Formulation for Parametric Size and Shape Optimization of Compliant Mechanisms," *Journal of Mechanical Design*, Vol. 121, No. 6, 1999, pp. 229–234.

[3] Bowman, J., Sanders, B., Cannon, B., Kudva, J., Joshi, S., and Weisshaar, T., "Development of next generation morphing aircraft structures," *AIAA 2007*, 48th AIAA/ASME/ASCE/AHS/ASC Structures, Structural Dynamics and Materials (SDM) Conference, Honolulu, Hawaii, 2007.

[4] Roth, B., Peters, C., and Crossley, W., "Aircraft sizing with morphing as an independent variable: motivation, strategies and investigations," *AIAA 2007*, 48th AIAA/ASME/ASCE/AHS/ASC Structures, Structural Dynamics and Materials (SDM) Conference, Honolulu, Hawaii, 2007.

[5] Barbarino, S., Bilgen, O., Ajaj, R. M., Friswell, M. I., and Inman, D. J., "A Review of Morphing Aircraft," *Journal of Intelligent Material Systems and Structures*, Vol. 22, 2011. doi:10.1177/1045389X11414084.

[6] Gomez, J. C., and Garcia, E., "Morphing Unmanned Aerial Vehicles," *Smart Materials and Structures*, Vol. 20, No. 10, 2011. doi:10.1088/0964-1726/20/10/103001.

[7] Ajaj, R. M., Saavedra Flores, E. I., Friswell, M. I., Allegri, G., Woods, B., Isikveren, A., and Dettmer, W., "The Zigzag Wingbox for a Span Morphing Wing," *Aerospace Science and Technology*, Vol. 28, No. 1, 2013, pp. 364 – 375. doi:10.1016/j.ast.2012.12.002.

[8] Griffin, K. E., and Hopkins, M. A., "Smart Stiffness for Improved Roll Control," *Journal of Aircraft*, Vol. 34, No. 3, 1997, pp. 445 – 447. doi:10.2514/2.2191.

[9] Chen, P. C., Sarhaddi, D., Jha, R., Liu, D. D., Griffin, K., and Yurkovich, R., "Variable Stiffness Spar Approach for Aircraft Maneuver Enhancement Using ASTROS," *Journal of Aircraft*, Vol. 37, No. 5, 2000, pp. 865 – 871. doi:10.2514/2.2682.

[10] Santer, M., and Pellegrino, S., "Topological Optimization of Compliant Adaptive Wing Structure," *AIAA Journal*, Vol. 47, No. 3, 2009, pp. 1080–1091. doi:10.2514/1.36679.

[11] Monner, H. P., Kintscher, M., Lorkowski, T., and Storm, S., "Design of a Smart Droop Nose as Leading Edge High Lift System for Transportation Aircrafts," *AIAA 2009–2128*, 50th AIAA/ASME/ASCE/AHS/ASC Structures, Structural Dynamics and Materials (SDM) Conference, Palm Springs, California, 2009.

[12] Kota, S., Hetrick, J. A., Osborn, R., Paul, D., Pendleton, E., Flick, P., and Tilmann, C., "Design and Application of Compliant Mechanisms for Morphing Aircraft Structures," *Volume 127*, SPIE – Smart Structures and Materials 2003: Industrial and Commercial Applications of Smart Structures Technologies, 2003, pp. 24 – 33. doi:10.1117/12. 483869.

[13] Arrieta, A. F., Bilgen, O., Friswell, M. I., and Ermanni, P., "Modelling and Configuration Control of Wing–Shaped Bi–Stable Piezoelectric Composites Under Aerodynamic Loads," *Aerospace Science and Technology*, Vol. 29, No. 1, 2013, pp. 453 – 461. doi:10.1016/j.ast.2013.05.004.

[14] Woods, B. K., and Friswell, M. I., "Preliminary Investigation of a Fishbone Active Camber Concept," *Volume 2: Mechanics and Behavior of Active Materials; Integrated System Design and Implementation*, Bio–Inspired Materials and Systems; Energy Harvesting: 555, 2012. doi:10.1115/SMASIS2012-8058.

[15] Ricci, S., and Terraneo, M., "Design, Manufacturing and Preliminary Test Results of an Adaptive Wing Camber Model," 47th AIAA/ASME/ASCE/AHS/ASC Structures, Structural Dynamics and Materials (SDM) Conference, Newport, Rhode Island, 2006, pp. 1–12.

[16] Miller, S., Vio, G. A., Cooper, J. E., Vale, J., da Luz, L., Gomes, A., Lau, F., Suleman, A., Cavagna, L., De Gaspari, A., Ricci, S., Riccobene, L., Scotti, A., and Terraneo, M., "SMorph – Smart Aircraft Morphing Technologies Project," *51th AIAA/ASME/ASCE/AHS/ASC Structures, Structural Dynamics and Materials (SDM) Conference*, AIAA 2010–2742, Orlando, Florida, 2010, pp. 1 – 14. doi:10.2514/6.2010-2742.

[17] De Gaspari, A., and Ricci, S., "A Two–Level Approach for the Optimal Design of Morphing Wings Based On Compliant Structures," *Journal of Intelligent Material Systems and Structures*, Vol. 22, No. 10, 2011, pp. 1091–1111. doi:10.1177/1045389X11409081.

[18] De Gaspari, A., and Ricci, S., "Knowledge–Based Shape Optimization of Morphing Wing for More Efficient Aircraft," *International Journal of Aerospace Engineering*, Vol. 2015, 325724, 2015, pp. 1 – 19. doi:10.1155/2015/325724.

[19] Diodati, G., Concilio, A., Ricci, S., De Gaspari, A., Huvelin, F., Dumont, A., and Godard, J., "Estimated Performances of an Adaptive Trailing Edge Device Aimed at Reducing Fuel Consumption on a Medium–Size Aircraft," *Industrial and Commercial Applications of Smart Structures Technologies (SPIE 2013)*, Vol. 8690, SPIE, Kevin M. Farinholt (Ed.), San Diego, CA, USA, 2013, pp. 1 – 16. doi:10.1117/12.2013685.

[20] De Gaspari, A., Ricci, S., Antunes, A., Odaguil, F., and Lima, G., "Chapter 6: Expected Performances," *Morphing Wing Technologies – Large Commercial Aircraft and Civil Helicopters*, Butterworth–Heinemann, 2018, pp.

175 – 203. doi:10.1016/B978-0-08-100964-2.00006-X, URL https://www.elsevier.com/books/morphing-wing-technologies/concilio/978-0-08-100964-2.

[21] Vasista, S., De Gaspari, A., Ricci, S., Riemenschneider, J., Monner, H., and van de Kamp, B., "Compliant Structures–Based Wing and Wingtip Morphing Devices," *Aircraft Engineering and Aerospace Technology*, Vol. 88, No. 2, 2016, pp. 311 – 330. doi:10.1108/AEAT-02-2015-0067.

[22] De Gaspari, A., Ricci, S., Antunes, A., Odaguil, F., and Rodrigues de Lima, G., "Application of Active Camber Morphing Concept to a Regional Aircraft," *22nd AIAA/ASME/AHS Adaptive Structures Conference (Scitech 2014)*, AIAA 2014–1259, Curran Associates, Red Hook, NY, National Harbor, Maryland, USA, 2014, pp. 167 – 189. doi:10.2514/6.2014-1259.

[23] Kroll, E., and Artzi, D., "Enhancing aerospace engineering students' learning with 3D printing wind–tunnel models," *Rapid Prototyping Journal*, Vol. 17, No. 5, 2011, pp. 393 – 402.

[24] Bubert, E. A., Woods, B. K., Lee, K., Kothera, C. S., and Wereley, N., "Design and Fabrication of a Passive 1D Morphing Aircraft Skin," *Journal of Intelligent Material Systems and Structures*, Vol. 21, 2010.

[25] Heyes, A., and Smith, D., "Rapid Technique for Wind–Tunnel Model Manufacture," *Journal of Aircraft*, Vol. 41, No. 2, 2003.

[26] Kulfan, B. M., "Universal Parametric Geometry Representation Method," *Journal of Aircraft*, Vol. 45, No. 1, 2008.

[27] Ansys, *Icem 12.1 Programmers Guide*, 2008. ANSYS, Inc.

[28] Lu, K.-J., and Kota, S., "An Effective Method of Synthesizing Compliant Adaptive Structures using Load Path Representation," *Journal of Intelligent Material Systems and Structures*, Vol. 16, 2005, pp. 307–317.

[29] Ghiringhelli, G. L., Masarati, P., and Mantegazza, P., "Multibody Implementation of Finite Volume C^0 Beams," *AIAA Journal*, Vol. 38, No. 1, 2000, pp. 131–138.

[30] Masarati, P., Morandini, M., and Mantegzza, P., "An Efficient Formulation for General-Purpose Multibody/Multiphysics Analysis," *ASME J. Comput. Nonlinear Dyn.*, Vol. 9, No. 4, 2014. doi:10.1115/1.4025628.

[31] De Gaspari, A., and Ricci, S., "Application of the Active Camber Morphing Concept Based on Compliant Structures to a Regional Aircraft," *Industrial and Commercial Applications of Smart Structures Technologies (SPIE 2014)*, Vol. 9059, SPIE, K. M. Farinholt, S. F. Griffin (Eds.), San Diego, CA, USA, 2014, pp. 1 – 21. doi:10.1117/12.2045225.

[32] Deb, K., *Multi–Objective Optimization Using Evolutionary Algorithms*, John Wiley & Sons, Inc., New York, NY, USA, 2009.

[33] Zanotti, A., and Gibertini, G., "Experimental Investigation of the Dynamic Stall Phenomenon on a NACA 23012 Oscillating Airfoil," *Proceedings of the Institution of Mechanical Engineers, Part G: Journal of Aerospace Engineering*, Vol. Vol. 227, No. No. 9, 2013.